Towards quantifying the effect of pump wave amplitude on cracks in the Nonlinear Coda Wave Interferometry method

Shilin Qu, Benoit Hilloulin, Olivier Chupin, Jean-Michel Piau, Odile Abraham, Vincent Tournat

Towards quantifying the effect of pump wave amplitude on cracks in the Nonlinear Coda Wave Interferometry method

Shilin QU[a,*], Benoît HILLOULIN[b], Olivier CHUPIN[c], Jean-Michel PIAU[c], Odile ABRAHAM[a], Vincent TOURNAT[d]

[a]*GERS-GeoEND, Université Gustave Eiffel, IFSTTAR, CS5004, F-44344 Bouguenais, France*
[b]*Nantes Université, Ecole Centrale Nantes, CNRS, GeM, UMR 6183, 1 rue de la Noë, 44321 Nantes, France*
[c]*LAMES-MAST, Université Gustave Eiffel, IFSTTAR, CS5004, F-44344 Bouguenais Cedex, France*
[d]*Laboratoire d'Acoustique de l'Université du Mans (LAUM), UMR 6613, Institut d'Acoustique - Graduate School (IA-GS), CNRS, Le Mans Université, France*

Abstract

In Non-Destructive Testing and Evaluation (NDT&E), an ultrasonic method called Nonlinear Coda Wave Interferometry (NCWI) has recently been developed to detect cracks in heterogeneous materials such as concrete. The underlying principle of NCWI is that a pump wave is used to activate the crack breathing which interact with the source probe signal. The resulting signal is then measured at receiver probes. In this work, a static finite element model (FEM) is used to simulate the pump wave/crack interaction in order to quantify the average effect of the pump waves on a crack. By considering both crack opening and closure phases during the dynamic pump wave excitation, this static model aims to determine the pump stress amplitude for a given relative crack length variation due to the dynamic pump wave excitation at different amplitudes. Numerical results show, after reaching a certain stress amplitude, a linear relationship between the relative crack length variation and the equivalent static load when considering a partially closed crack at its tips. Then, numerical NCWI outputs, e.g., the relative velocity change θ and the decorrelation coefficient K_d, have been calculated using a spectral element model (SEM). These results agree with previously published experimental NCWI results derived for a slightly damaged 2D glass plate.

Keywords: concrete, coda, nonlinear acoustics, crack breathing, ultrasound, finite element method, spectral element method, NCWI

1. Introduction

Background

Cracks are often considered as one of the most impactful features in civil structures, as they induce a strength loss and reduce durability.Cracks can be generated by fatigue loadings [1], chemical attacks [2, 3] or shrinkage [4–6]. In the field of the NDT&E of heterogeneous

*Corresponding author
Email addresses: shilin.qu@univ-eiffel.fr (Shilin QU), benoit.hilloulin@ec-nantes.fr (Benoît HILLOULIN)

materials like concrete, elastic waves with wavelengths comparable to the size of heterogeneities are scattered multiple times by the heterogeneities, resulting in the generation of the coda wave [7–11]. These coda waves analysis constitutes a powerful tool for detecting cracks thanks to its high sensitivity (temperature) [12] , minor mechanical evolution (e.g. cracks) [13–15]. This is because the trajectory of coda waves is much longer than ballistic waves due to multiple scattering. The cumulative effect during the traveling time makes coda waves highly sensitive to media changes even when they are weak. A linear ultrasonic NDT&E technique, called Coda Wave Interferometry (CWI) has been developed in order to detect micro damage, e.g. cracks formed between aggregates and mortar in concrete [13, 16, 17] or other complex media [18–21], or to monitor the health of structures over the long term [12, 15, 22–25].

Principle of CWI

In CWI, the principle consists of comparing coda signals in different material states. A sweep sine signal, whose wavelengths are comparable to the size of the heterogeneities, serves as a source to generate coda signals. A reference coda is recorded at an initial state (e.g. the intact state), and a perturbed coda is recorded at another state (e.g. damaged state). The appearance of cracks leads to two major effects: 1) a local decrease in the Young's modulus around the cracks, hence a small decrease in wave velocity; and 2) a modification of the scattering property of elastic waves. These two effects can be quantified by two CWI observables θ and K_d, retrieved from the reference and perturbed coda signals by applying the stretching method [26, 27]. θ represents the relative velocity change of the elastic medium while K_d represents the decorrelation coefficient between reference and perturbed coda signals. However, CWI has several drawbacks. First, it requires a reference state (usually expected on an intact sample), which is not always realistic. Second, CWI cannot detect defects, including closed cracks, that may also exist in concrete structures [28]. In order to improve CWI, a nonlinear ultrasonic NDT&E technique, called NCWI, has been developed based on CWI.

Principle of NCWI

In NCWI, a series of high-amplitude low-frequency (LF) dynamic pump waves $\sigma_{dyn}(t)$, typically a sine sweep with varying maximum amplitude, denoted $\sigma_{dyn}^{max} = |max(\sigma_{dyn}(t))|$ in the following, is used to generate local nonlinearities around the cracks, especially closed cracks, via the crack breathing effect. The frequency range of the pump waves usually covers the first 50 modal frequencies of the inspected sample in order to achieve an equipartition of energy of pump waves in the media. During pump wave excitation, multiple desynchronized low-amplitude high-frequency (HF) probe waves, whose wavelength is close to the size of the heterogeneities found in the medium, are used to generate coda waves. The application of LF pump waves and HF probe waves over a crack induces two semi-coupled dynamic phenomena: 1) interaction between pump wave and cracks (e.g. crack breathing), 2) interaction between probe wave and breathing of cracks. Similarly to CWI, NCWI also needs a reference state and a perturbed state. In NCWI, the reference state is when the pump is switched off, the reference coda is then compared with a perturbed coda, whose pump amplitude is nonzero. Thus, NCWI is free of the need for an intact sample to serve as the reference state. In addition, the positive and negative pump wave amplitudes will close and open the crack

tips, thus producing the crack breathing effect. This effect makes NCWI sensitive to closed cracks [29, 30]. Experimental observations have shown that θ and K_d follow respectively a linear and quadratic relation with respect to pump stress amplitude, which yields two NCWI observables, namely α_θ and α_{K_d}. α_θ and α_{K_d} represent respectively the coefficient of linear and quadratic terms of θ and K_d with respect to pump stress amplitude. These terms reflect the level of nonlinearity of the inspected sample and can be used as criteria of the global damage level. Despite these improvements, NCWI also displays some drawbacks. For instance, in a large structure, it is difficult to obtain an equipartition of pump wave energy inside the structure, which means that the nonlinearity induced by certain defects is less than expected or even incapable of being excited by pump waves.

Crack imaging

Over the past few years, numerous works have focused on both the numerical [31–33] and the experimental [29, 30, 34–40] aspects of CWI and NCWI. However, both are only able to detect and evaluate the damage level of a material at the global level in a comparative manner. It can not localize the defects. Therefore, the need for imaging techniques based on NCWI has become more acute. Various techniques exist to image defects in complex media, e.g. X-ray tomography [41], 2D/3D microscopy [42], air-coupled time reversal mirror [43]. However, these techniques are unable to image weak changes such as microcracking, especially in very heterogeneous media. The localization of weak changes using diffuse waves (LocaDiff) [44–47] with CWI has been under study for the past ten years. LocaDiff is an imaging algorithm founded on a diffusive propagation model and a maximum likelihood approach. It requires a reference state and uses an analytical solution for the scattering cross section. A combination of CWI and Time Reversal (TR), called CWI-TR, which eliminates the need for intact samples and allows for the detection of closed cracks, has recently been investigated in [48]. According to this method, TR is employed with multiple pump wave generators to refocus pump waves at specific points so as to activate crack nonlinearity. CWI is performed at the same time in order to form a map of CWI observables. However, the refocused pump wave has a limited detection zone, i.e. at or around just the shallow surface, which means only surface-breaking cracks or shallow subsurface cracks can be detected. It is expected that a combination of the LocaDiff methodology and NCWI will enable the 3D imaging of closed cracks and/or cracks without requiring a reference sample.

The imaging process is founded on (1) a model space and (2) a measurement space. The model space contains model parameters that can be estimated theoretically. The measurement space contains measurement parameters that are given by experiments. The inverse problem consists in recovering the model parameters from the measurement parameters. In the case of LocaDiff with CWI, the measurement parameters are the experimental relative velocity variation θ and the decorrelation coefficient K_d and the corresponding model parameters are the intrinsic relative velocity variation $\delta v/v$ and the scattering cross section of the crack σ_D [47], where σ_D represents the scattering ability of a defect. This term is equal to the ratio of scattered energy flux to the incident energy flux [49–52]. Although LocaDiff can be performed with both measurement parameters [47], the majority of existing works relies on K_d for the inversion [44–46]. Therefore, the use of K_d and σ_D will be preferred in the following during this study.

Static models: pump wave/crack interaction

In an attempt to combine LocaDiff with NCWI, it is anticipated to introduce a dependency of the pump stress amplitude on the scattering cross section of a crack σ_D. The aim of the forward problem therefore is to relate σ_D to the pump stress amplitude σ_{dyn}^{max}. Recent experimental works have shown that θ and K_d obeys a linear relation and a quadratic relation with the pump stress amplitude [30, 34, 35]. According to the numerical study of [31], these relations can be reproduced numerically by considering cracks at different relative crack length variation $\widetilde{dL/L}$, where dL represents the algebraic crack length variation at crack tip that is equivalent to the average effect of dynamic pump stress waves during the crack breathing on the crack tips. Therefore, different $\widetilde{dL/L}$ represent the average effect of different pump stress amplitudes. The relation between the σ_{dyn}^{max} and σ_D can be found by firstly getting the relation between σ_{dyn}^{max} and $\widetilde{dL/L}$ then replace $\widetilde{dL/L}$ with its corresponding σ_D. However, the real pump stress wave excitation involves the interaction of elastic waves with cracks which is a dynamic process. Furthermore, the resulting crack breathing effect involves an unilateral contact problem which is relatively complicated to model. Different models have been proposed in order to model the crack/elastic wave interaction such as: realistic morphology model [53], pillar model [54] and mass-spring model [55]. These models contain numerous parameters which can be difficult to recover in an inverse problem and some of them are difficult to measure experimentally. Due to this reason, in order to develop a robust inverse method for closed crack detection in very heterogeneous materials, a model which contains as less parameters as possible is to be preferred.

In this paper, a simplified Finite Element (FE) static model is proposed which brings the dynamic problem involved in the crack breathing activated by the dynamic pump wave down to a quasi-static problem.

This article is presented in three parts. In the first part, the motivation of the study and the main steps of the models will be presented. In the second part, the methodology of the static model and the numerical NCWI model (via SEM2D [56, 57]) are introduced first. Then, a comparison between numerical and experimental NCWI results is proposed in order to validate the protocol of the static model. In the last part, the results of the improved static model and the results of NCWI model are presented in order to show firstly the relation between σ_{dyn}^{max} and $\widetilde{dL/L}$ and then the relations of θ and K_d with respect to σ_{dyn}^{max}.

2. Motivation of the study

In NCWI, the LF pump waves can activate the crack breathing effect, whereby crack tips open and close alternatively. To detect the crack breathing effect, multiple desynchronized HF probe waves are sent into the medium at the same time as the dynamic pump waves in order to generate coda waves. The coda waves at a zero pump amplitude are set as the reference coda, while the coda waves at different nonzero pump amplitudes are taken as the perturbed coda. Then, θ can be calculated at each pump amplitude according to the

stretching method [26, 27] (Eq. 1):

$$CC(\theta_n) = \frac{\int_{t_1}^{t_2} u_i(t(1+\theta_n))u_p(t)dt}{\sqrt{\int_{t_1}^{t_2} u_i^2(t(1+\theta_n))dt \int_{t_1}^{t_2} u_p^2(t)dt}}, \tag{1}$$

where $u_i(t)$ and $u_p(t)$ denote the reference and perturbed codas, respectively and t_1, t_2 are the beginning and the end of the time integration window. The final value of θ is the one that maximizes $CC(\theta_n)$. The decorrelation coefficient K_d is calculated using the following equation:

$$K_d = 100(1 - CC(\theta)). \tag{2}$$

Recent research has shown that the change in CWI observables θ and K_d due to the crack breathing effect resulting from the dynamic stress pump wave can be reproduced by a simple change in crack length ratio $\widetilde{dL/L}$ [31]. Hence, a numerical model which can give the relation between the relative crack length variation $\widetilde{dL/L}$ and the maximum dynamic stress pump wave amplitude σ_{dyn}^{max} in NCWI is the goal of this study. The layout of this paper that demonstrates the step-by-step procedure to achieve this goal is represented in Fig.1:

1. static modeling using FEM that models both the opening and closure of a crack under a far field stress σ_{yy}^{ff} corresponding to the pump effect, which gives the relationship between $dL^{\pm}/L$ and σ_{dyn}^{max} where dL^{-}/L and dL^{+}/L represent the relative crack length variation in closure and opening cases respectively,
2. use of the relation between σ_{yy}^{ff} and $dL^{\pm}/L$ to convert the dynamic pump stress waves signal $\sigma_{dyn}(t)$ into transient relative crack length variation $[dL/L]_{dyn}(t)$,
3. time average of $[dL/L]_{dyn}(t)$ and establishment of the relation between σ_{dyn}^{max} and $\widetilde{dL/L} = \frac{1}{L\Delta_t}\int_0^{\Delta_t} dL(\sigma_{dyn}(t))dt$ where Δ_t is the duration of the coda acquisition,
4. application of cracks at different $\widetilde{dL/L}$ in numerical simulation of NCWI via SEM2D, and qualitative comparison of the relations between θ and K_d vs. $\widetilde{dL/L}$ with experimental NCWI results.

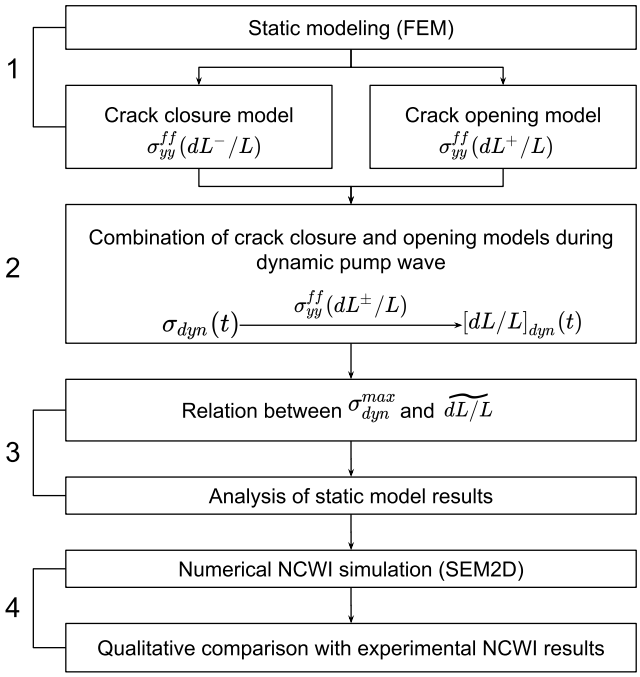

Figure 1: Workflow of the study.

3. Modeling methodology

3.1. Static model

The physical description of crack breathing is the alternation between open and close states of crack tips due to external excitation. Therefore, the crack displacement for a given far field stress equivalent to the pump effect is looked for in the static modeling. The crack displacement is calculated numerically using a simplified 2D model (plane strain) of a single crack embedded into an infinite homogeneous elastic medium The crack geometry is considered with an initial opening under no stress condition and verifies the following equation: $y = \pm y_{geo(x)} = \pm\frac{h}{4}(1+\cos(\pi\frac{2x}{L}))$ with $0 \leq x \leq L/2$, $0 \leq y_{geo} \ll D$ and $y_{geo}(-x) = y_{geo}(x)$ where h is the aperture at the crack center and L the length of the crack.(see Fig.2). This FE static model entails several imposed hypotheses, namely:

1. symmetry with x and y of the whole problem (geometry, loading, boundary conditions),
2. small strains and displacements,
3. the equivalent static load is biaxial,
4. the crack is considered to have some initial opening, but with tangent crack tips at $x = \pm L/2$,
5. the dimension of the meshed domain is large enough to be equivalent to an infinite medium,
6. the medium under the stress pump wave at each time step can be considered as a static problem.

Under the above hypothesis, a FE model will be constructed using the software *FreeFEM++* [58] to establish the relation between σ_{dyn}^{max} and $\widetilde{dL/L}$ which will subsequently be related to a given dynamic pump waves amplitude. A detailed description of the static model is provided in Appendix B.

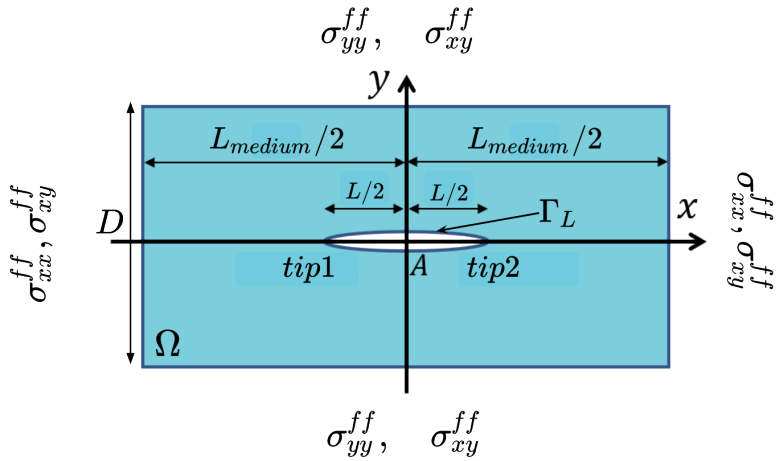

Figure 2: Schematics of the finite 2D rectangular domain Γ of dimension $L_{medium} \times D$ with a partially closed crack Γ_L centered at the center point A, the 2D domain is subjected to a far field stress $\boldsymbol{\sigma^{ff}}$ on the boundaries.

3.2. Crack closure and crack opening

In order to simulate the interaction between the pump wave and the crack, both crack closure and crack opening need to be considered, as illustrated in Fig.3, which correspond to the crack under compression and tension respectively. The crack closure is modeled via a sub-problem decomposition method detailed in Appendix C. The crack closure process is used to obtain the relation between the far field compressive stress σ_{yy}^{ff} and the crack closure length dL^-, whereas the crack opening problem is directly solved by applying a far field tensile stress in the numerical model. The crack has a curved shape ending with a straight line with zero aperture. The junction between both parts is smooth with a curvature radius R defined as:

$$\frac{1}{R} = \left.\frac{d^2y}{dx^2}\right|_{x=L/2} \tag{3}$$

Given the geometry of the crack expressed in the previous section, $R = L^2/(\pi^2 h)$. Thus h will be later used as a main parameter to assess the influence of the crack geometry on the results. A geometrical parameter named the limit aperture of the crack denoted ω is introduced to determine the crack opening length dL^+ that deals with a pre-close crack segment denoted dL_{pre}.

3.3. Implementation of the static model

The modeling is applied to an experimental NCWI configuration made with glass, described in [59]. The elastic characteristics of the glass are presented in Table 1. As per the theoretical description, the size of the finite 2D model is considered infinite relative to the

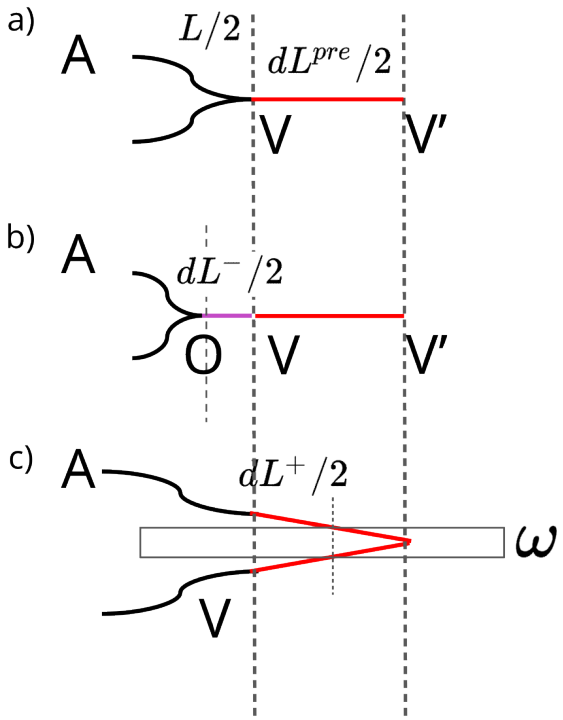

Figure 3: Crack states: a) initial , b) closed , c) open.

crack length. Therefore, a minimum sample size needs to be determined such that σ_{yy}^{ff} will be independent of this size. Various theoretical sizes were investigated. As illustrated in Fig.4, σ_{yy}^{ff} can be considered stable from $L_{medium} = 100\,\text{mm}$. Therefore, L_{medium} is fixed at a secured value of 300 mm in the following.

$\rho(kg/m^3)$	E(GPa)	ν	$V_p(m/s)$	$V_s(m/s)$
2500	69	0.25	5755	3323

Table 1: Elastic characteristics of glass

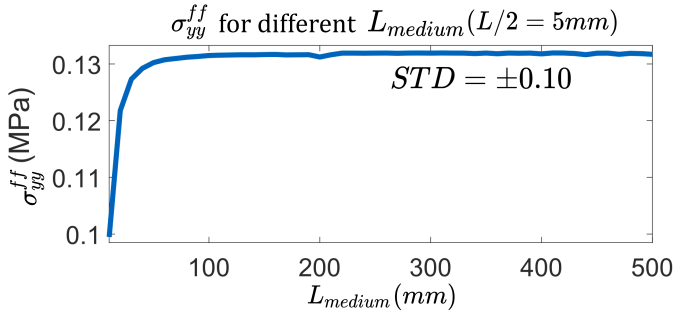

Figure 4: External normal stress σ_{yy}^{ff} applied on top of the medium (at segment $A'B'$) with respect to the medium size L_{medium}, with $L/2 = 5mm$, $dL = 0.1mm$, $h/2 = 5\mu m$ and $D = L$, STD stands for standard deviation

.

Since the half crack's aperture $h/2$ is $5\mu m$, the order of magnitude of the vertical displacement along the crack surface due to σ_{dyn}^{max} will not be greater than 10^{-6}m, which is much smaller compared to the medium's size L_{medium} 300mm. In order to avoid abrupt change in the size of element of the mesh around crack tip, a uniformly refined rectangle submesh of size 7.5 mm×25 µm covering the crack segment VA is added, while the segments' size along adjacent borders follow a logarithmic growth which guarantees a smooth transition. The final mesh employed is shown in Fig.5.

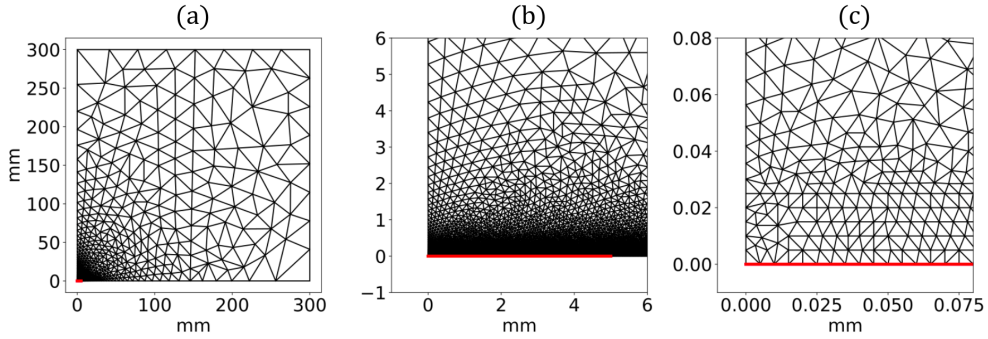

Figure 5: Schematic of the 300 mm×300 mm mesh used in the FE simulation, with $L/2 = 5$ mm and $h/2 = 5$ µm: a) total mesh, the crack segment is marked by the red line, b) zoom on the crack segment (red line), c) zoom on the left corner of the rectangular refined mesh.

3.4. Tools for numerical modeling of NCWI and validation process

The numerical modeling of NCWI is performed with the software SEM2D [60]. The Spectral Element Method (SEM) is often considered to be a derivation of FEM, which is also based on a weak formulation. Yet SEM displays advantages in solving Partial Differential Equations (PDE) via higher-order polynomial interpolation functions at a low numerical cost [61, 62]. At high-order interpolations, SEM can exhibit a fast spectral convergence and low numerical dispersion [63, 64] which is suitable for simulating HF wave propagation. In our case, the minimum element size needed to obtain spectral convergence lies between 4 mm

and 8mm. In order to validate the static model, a comparison between numerical NCWI results (θ and K_d versus pump amplitude) by use of the deformed crack at different $\widetilde{dL/L}$ values obtained from the static model with experimental ones has been undertaken. θ can be obtained from Eq.1 and Eq.3. The configuration of the numerical model with crack geometry at different $\widetilde{dL/L}$ obtained thanks to the static model is presented in Fig.6. The values of $\widetilde{dL/L}$ need to be related to given pump amplitudes. A 200mm×200mm squared 2D homogeneous glass plate is used as the medium of propagation. A crack at 9 different $\widetilde{dL/L}$ (from 0.0% to 8.0% with a step of 1.0 %, L=10mm, h=10μm at unclosed state) is placed in a circle whose radius is 25mm centered at x = 155mm and y = 140mm. A high-frequency sweep sine from 200kHz to 800kHz during 0.2ms is used as probe wave source which is located at x = 50mm and y = 0mm. Each boundary has 9 receivers with a 4-ms acquisition duration. In order to demonstrate the robustness of the numerical model with respect to both crack location and orientation, 5 crack locations and orientations are randomly chosen inside the orange circle, as presented in Fig.7. The final NCWI results will be calculated as the average over these 5 random selections with corresponding errors at each pump amplitude.

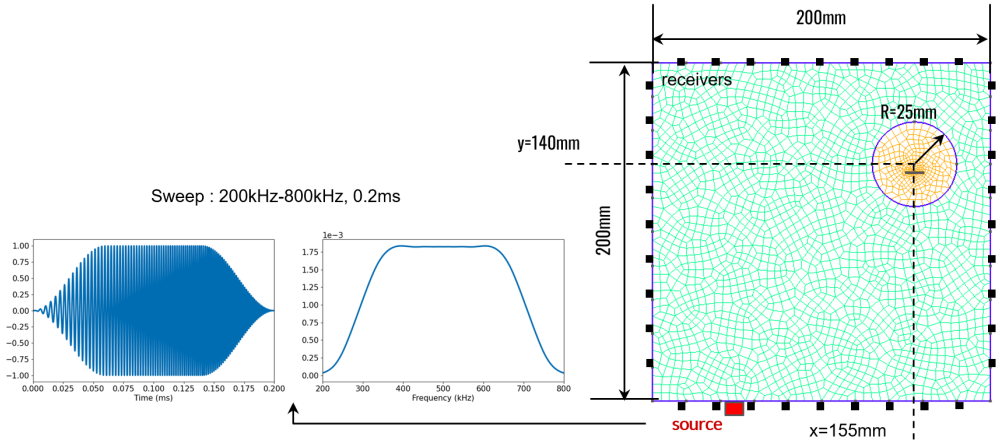

Figure 6: Schematics of the numerical model of NCWI: homogeneous 2D glass plate (200mm×200mm), a sweep type source ranging from 200kHz to 500kHz during 0.2ms located at x=50mm and y=0mm, 9 receivers are placed at each border with 20mm spacing between each of them. The orange circular zone located at x=155mm and y=140mm represents the zone which limits the position of the crack during the random selection process.

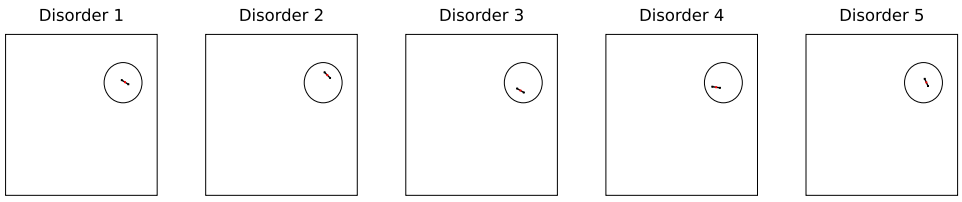

Figure 7: Schematic of the geometry of homogeneous 2D glass plate (200mm×200mm) containing one crack of 10mm in length and of 10 μm in aperture over 5 random selections of the crack position and its orientation.

4. Results and discussion

4.1. Static model results

The results of the parametric study on adimensionnal analysis of crack closure are presented in Fig.8. As shown in Appendix B.1, the relative crack length variation depends only on σ_{yy}^{ff}. Therefore, in the following, $\boldsymbol{\sigma^{ff}}$ is replaced by σ_{yy}^{ff} and is inferred as the instant stress amplitude of the dynamic pump wave at moment t_i ($\sigma_{dyn}(t_i)$). It can be noticed that σ_{yy}^{ff}/E obeys a quadratic relation with respect to dL^-/L and a linear relation with respect to h/L, which means that the dependency on h/L could be characterized by a single constant coefficient thanks to its linearity with respect to σ_{yy}^{ff}/E.

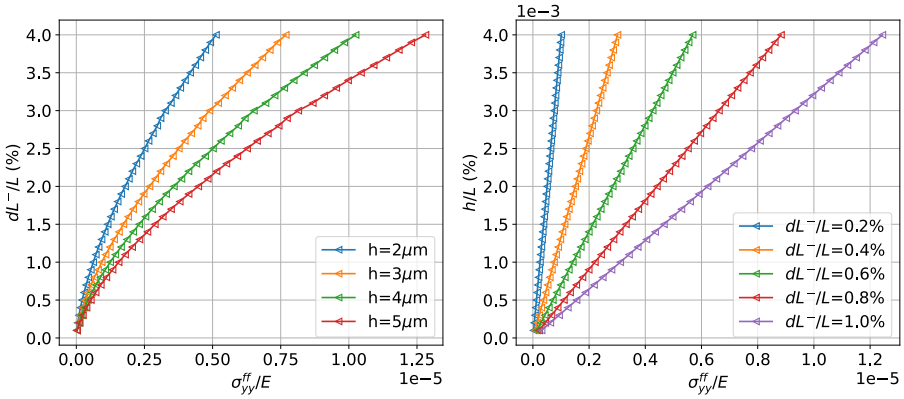

Figure 8: Variation of the normalized far field normal stress σ_{yy}^{ff}/E with respect to a) crack closure dL^-/L and, b) normalized crack's aperture h/L.

In Fig.9, it can be noticed that σ_{yy}^{ff}/E obeys an irregular relation with respect to crack opening dL^+/L, which is related to the deformation of the crack. Four dL^{pre}/L are chosen in order to perform the paramatric study on ω/h. In the crack opening case, $\omega/2$ is not allowed to be greater than the crack aperture at point V, $u_y(V)$. Therefore, for each dL^{pre}/L, the value of ω/h varies between 0 and the maximum value $\omega/h = 2u_y(V)/h$.

It is worth noting that for each value of dL^{pre}/L, the maximum of ω/h chosen is different. This is due to different normal displacement at point V, $u_y(V)$, for a given σ_{dyn}^{max} at different dL^{pre}/L. When $\omega/h = 0$, the pre-close part is considered completely open once $\sigma_{dyn}(t) > 0$. When $\omega/h > 0$, the value of dL^+/L stays at 0 at the beginning because the normal displacement at point V (or the crack aperture at point V) under weak tension is still smaller than the given ω. Once this criteria is reached, dL^+/L becomes positive and the crack is considered opened. The greater the value of ω/h is, the higher the tensile stress is required to reach crack opening. The relation between ω/h and the required tensile stress for crack opening is linear.

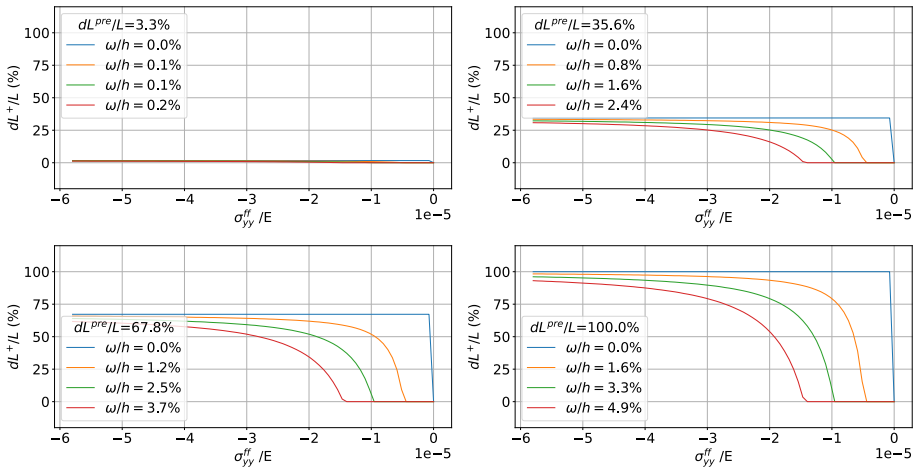

Figure 9: Variation of dL^+/L with respect to the far field normalized normal stress σ^{ff}_{yy}/E at different preclosure length dL^{pre} and limit aperture ω.

Using the relation between σ^{ff}_{yy}/E and $dL^{\pm}/L$ found in Figures 8 and 9, the dynamic amplitude of pump waves (Fig. 10 left) can be converted to $[dL/L]_{dyn}$ (Fig. 10 right) which is time-dependent. An example of this conversion is presented in Fig.10.

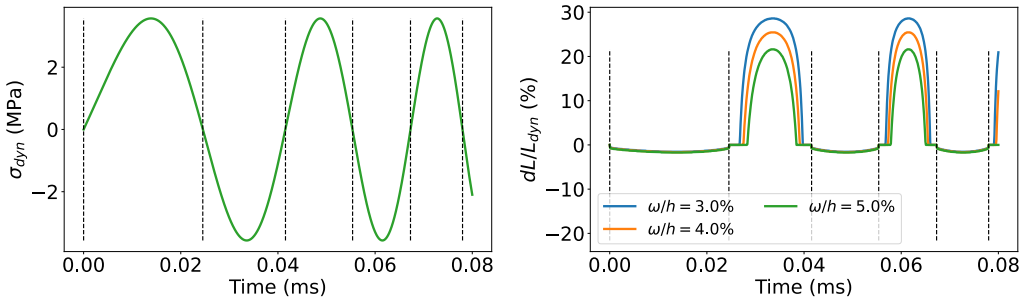

Figure 10: Left: zoomed chirp signal (0.08ms over 11ms) of the dynamic stress pump wave at σ^{max}_{dyn} =3.56MPa (pump wave is a sine sweep that varies in time, the positive part represents the compressive state where the crack is closed, and the negative part represents the tensile state where the crack is open). Right: calculation of the instant relative crack length variation $[dL/L]_{dyn}$ of dynamic stress pump wave at different limit aperture ω at σ^{max}_{dyn} =3.56MPa, $dL^{pre}/L = 30\%$.

After converting the dynamic pump wave's amplitude into $[dL/L]_{dyn}(t)$, the time average of $[dL/L]_{dyn}$ during the coda acquisition time (4 ms), denoted $\widetilde{dL/L}$, can be calculated. Fig.11 shows the results of $\widetilde{dL/L}$ at different ω/h. It is observed that the overall averaged effect of the dynamic pump wave excitation on a pre-close crack is equivalent to crack opening. This result is in agreement with the numerical NCWI results in [31]. Besides, a linear relation between $\widetilde{dL/L}$ and σ^{max}_{dyn} is found, which satisfies the last hypothesis imposed in section 3.1. This relation will be used later on to perform the conversion from $\widetilde{dL/L}$ to σ^{max}_{dyn} during the numerical NCWI modeling. However, due to the application of ω, a certain initial stress amplitude is required in order to consider the crack as opened, such need of initial stress is

observed numerically and experimentally in wave/crack interaction [65, 66] in order to open a closed crack. The value of this initial stress depends on ω and dL^{pre}. The determination of ω and dL^{pre} is rather flexible regarding the fact that the linearity between $\widetilde{dL/L}$ and σ_{dyn}^{max} is preserved whatever the values of ω and dL^{pre} are. Also, the non uniform relation between σ_{dyn}^{max} and $\widetilde{dL/L}$ after the application of ω implies that the level of non-linearity depends on the initial crack aperture. It will be demonstrated in the next section that the values of ω and dL^{pre} can be determined as long as the numerical NCWI results are quantitatively in agreement with experimental results.

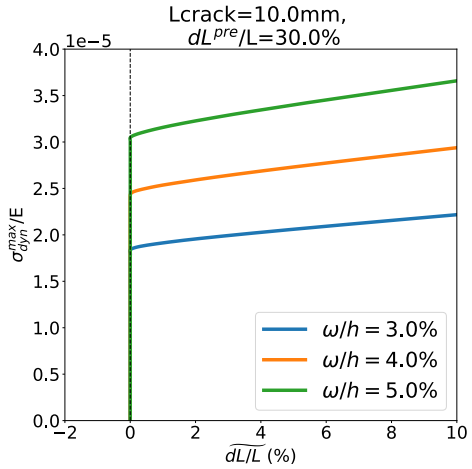

Figure 11: Results of σ_{dyn}^{max} with respect to $\widetilde{dL/L}$ for a crack of L =10mm and $dL^{pre}/L = 30\%$ at 3 different ω/h (3.0%, 4.0% and 5.0%). A certain amplitude of σ_{dyn}^{max}/E is required to trigger the crack opening. This value equals to 1.8 (1.2MPa), 2.4 (1.7MPa) and 3.0 (2.1MPa) respectively to the 3 chosen ω/h.

4.2. Numerical NCWI results

The numerical coda signals at 5 different $\widetilde{dL/L}$ values (0.0%, 1.0%, 3.0% 5.0%, 7.0%), presented in Fig.12 show that the greater the value of $\widetilde{dL/L}$, the greater the coda signal dilatation and decorrelation relative to the reference coda. Since the current results are applicable for just one crack, the modification is rather weak. However with NCWI, even these weak changes can be quantified with precision.

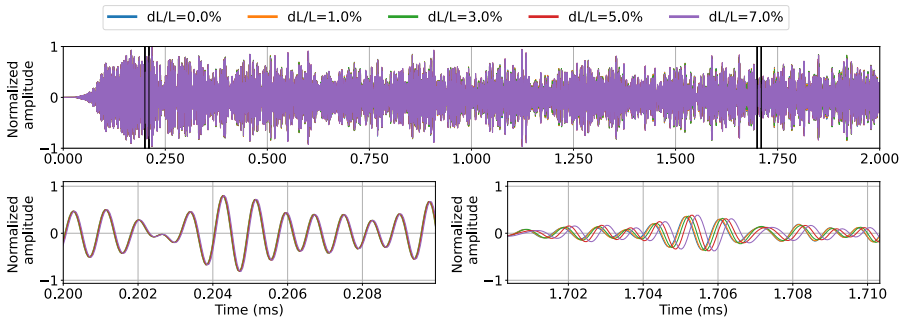

Figure 12: Numerical coda signals obtained at 5 different $\widetilde{dL/L}$ (0.0%, 1.0%, 3.0% 5.0%, 7.0%) for a cosine-like crack of L=10mm, h=10μm inside a 200 mm×200 mm 2D glass plate.

The numerical NCWI simulation results are presented in Fig.13. The values of θ and K_d are averaged over 5 disorders at each $\widetilde{dL/L}$ value. These results reveal a linear and a quadratic relation between θ, K_d, respectively. The orders of magnitude of θ and K_d are 10^{-3} and 10^{0}, respectively. These observations are in agreement with the experimental results found for a weakly damaged glass plate [59]. Moreover, it is observed that the standard deviation of θ and K_d increase with $\widetilde{dL/L}$. This finding may be correlated with the sensitivity of wave/crack interactions to crack position and orientation: the modification of wave propagation trajectories is cumulative during propagation. The geometrical change in the crack can modify its surface inside as well as its scattering property. These two modifications will lead to changes in the effective coda wave velocity and waveform distortion, which ultimately change the values of θ and K_d. Therefore, as $\widetilde{dL/L}$ increases, the changes of θ and K_d become more pronounced.

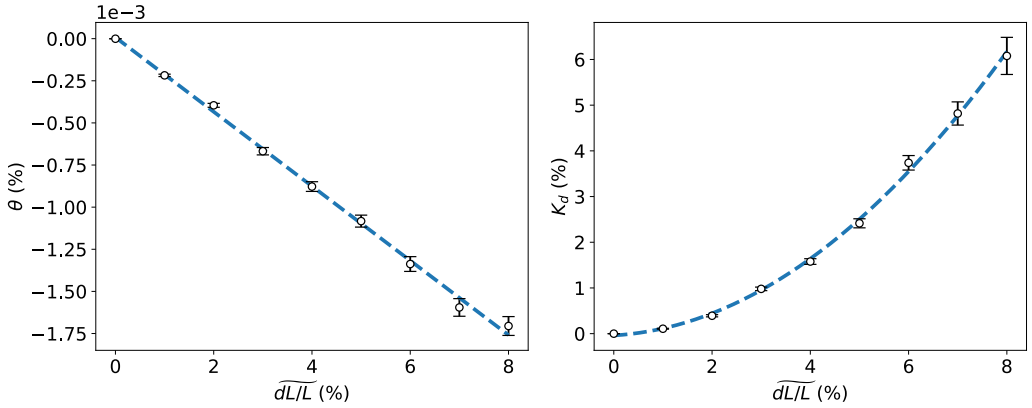

Figure 13: Numerical NCWI result: $\theta(\widetilde{dL/L})$ et $K_d(\widetilde{dL/L})$ for a crack at length of 10mm and at aperture of 10 μm in a glass plate of 200mm×200mm averaged over 5 disorders in crack's position.

Then, an estimation of σ_{dyn}^{max} by using the relation between $\widetilde{dL/L}$ and σ_{dyn}^{max} found in Fig.11 for a crack of 10mm of length and $dL^{pre} = 30\%$ is presented in this section. This single parameter set choice is due to the linearity observed previously in dL^{pre} and ω/h with respect to $\widetilde{dL/L}$. The NCWI result after conversion from $\widetilde{dL/L}$ to σ_{dyn}^{max} is shown in Fig.14. Since $\widetilde{dL/L}$ is linear to σ_{dyn}^{max}, the linear and quadratic relations of θ and K_d with respect to σ_{dyn}^{max} is preserved. Due to the requirement of an initial stress to reach the open crack state (Fig.11), σ_{dyn}^{max}/E does not start from zero. For the choice of $\omega/h = 5\%$ and $dL^{pre} = 30\%$, this initial stress is of $\sigma_{dyn}^{max}/E \approx 3.0$ (or 2.1MPa). In NCWI, the pump strain is at an order of magnitude around 10^{-5}, which corresponds to around 1MPa in a glass plate. This stress amplitude is smaller than 2.1MPa, but thanks to the static model, this value can be tuned to needed amplitude by varying ω/h and $dLpre/L$.

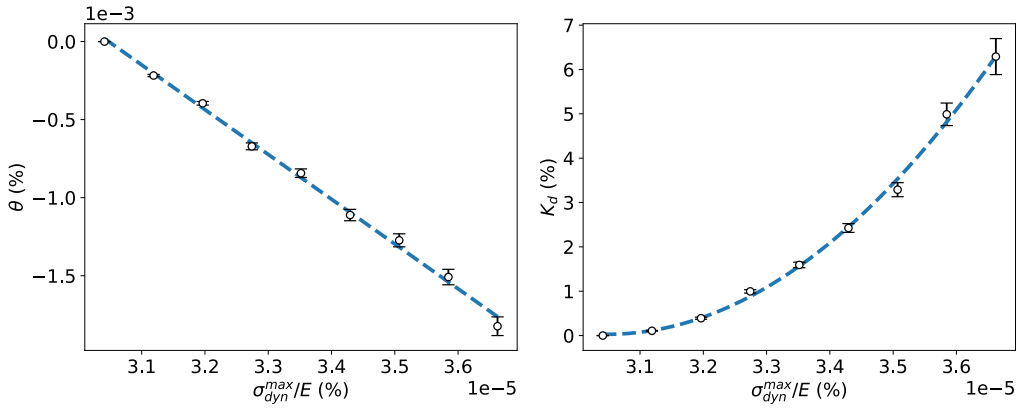

Figure 14: θ and K_d with respect to σ_{dyn}^{max}/E for a crack with $\omega/h = 10\%$ and $dL^{pre} = 100\%$.

5. Conclusion and perspectives

This study has investigated the average effect of dynamic pump waves on cracks in Nonlinear Code Wave Interferometry (NCWI) inside a finite 2D homogeneous medium using a simplified static finite element model. A time average of the relative crack length variation over the dynamic pump wave, with a given value of the initial external load, has been used due to the application of the limit aperture ω during both crack opening and closure. A 2D Spectral Element model has been implemented to simulate the influence of a crack in a 2D homogeneous reverberating medium on NCWI results. According to these results, the following main conclusions can be drawn:

- The static model contains five adimensional parameters: $\widetilde{dL/L}$, σ_{dyn}^{max}/E, h/L, dL^{pre}/L and ω/h. Since the relative crack length variation $\widetilde{dL/L}$ is what is looked for and σ_{dyn}^{max}/E is imposed initially during NCWI, therefore, this static model can properly work by only tuning the other three parameters, which can be useful for purposes of inversion.

- Linear relations between the maximum dynamic pump stress wave amplitude σ_{dyn}^{max} and the relative crack length variation $\widetilde{dL/L}$ have been found for a crack of L=10mm and h=10μm at different limit aperture ω/h by considering both crack closure and crack opening during the dynamic pump wave excitation.

- The numerical NCWI results were compared to experimental measurements in a 2D glass plate: the relative velocity variation of the medium θ is linear to σ_{dyn}^{max}/E and the coefficient of decorrelation K_d is quadratic to σ_{dyn}^{max}/E. The standard deviation of θ and K_d increases with the relative crack length variation $\widetilde{dL/L}$ due to the accumulated change in wave propagation trajectories.

In conclusion, this study has provided the possibility to simulate the equivalent average effect of dynamic pump waves in NCWI on a single crack by use of a simplified static model containing only three parameters: h/L, dL^{pre}/L and ω/h. Thanks to the applied hypothesis, this simplified model enables imaging quantitatively cracks with NCWI.

References

[1] H. Horii, H. C. Shin, T. M. Pallewatta, Mechanism of fatigue crack growth in concrete, Cement and Concrete Composites 14 (2) (1992) 83–89, special Issue on Micromechanics of Failure in Cementitious Composites. doi:https://doi.org/10.1016/0958-9465(92)90002-D.
URL https://www.sciencedirect.com/science/article/pii/095894659290002D

[2] G. Giaccio, R. Zerbino, J. Ponce, O. Batic, Mechanical behavior of concretes damaged by alkali-silica reaction, Cement and Concrete Research 38 (7) (2008) 993–1004. doi:https://doi.org/10.1016/j.cemconres.2008.02.009.
URL https://www.sciencedirect.com/science/article/pii/S0008884608000537

[3] X. Brunetaud, R. Linder, L. Divet, D. Duragrin, D. Damidot, Effect of curing conditions and concrete mix design on the expansion generated by delayed ettringite formation, Materials and Structures 40 (6) (2007) 567–578.

[4] K. Wiegrink, S. Marikunte, S. P. Shah, Shrinkage cracking of high-strength concrete, Materials Journal 93 (5) (1996) 409–415.

[5] Y. Akkaya, C. Ouyang, S. P. Shah, Effect of supplementary cementitious materials on shrinkage and crack development in concrete, Cement and Concrete Composites 29 (2) (2007) 117–123. doi:https://doi.org/10.1016/j.cemconcomp.2006.10.003.
URL https://www.sciencedirect.com/science/article/pii/S0958946506001818

[6] J. Kheir, A. Klausen, T. Hammer, L. De Meyst, B. Hilloulin, K. Van Tittelboom, A. Loukili, N. De Belie, Early age autogenous shrinkage cracking risk of an ultra-high performance concrete (uhpc) wall: Modelling and experimental results, Engineering Fracture Mechanics 257 (2021) 108024. doi:https://doi.org/10.1016/j.engfracmech.2021.108024.
URL https://www.sciencedirect.com/science/article/pii/S0013794421004458

[7] K. Aki, B. Chouet, Origin of coda waves: Source, attenuation, and scattering effects, J. Geophys. Res. 80 (23) (1975) 3322–3342. doi:10.1029/JB080i023p03322.
URL https://agupubs.onlinelibrary.wiley.com/doi/abs/10.1029/JB080i023p03322

[8] L. Margerin, Coherent Back-Scattering and Weak Localization of Seismic Waves, Adv. Geophys. 50 (08) (2008) 1–19. doi:10.1016/S0065-2687(08)00001-0.

[9] J. de Rosny, A. Tourin, M. Fink, Observation of a coherent backscattering effect with a dipolar source for elastic waves: Highlight of the role played by the source, Phys. Rev. E - Stat. Physics, Plasmas, Fluids, Relat. Interdiscip. Top. 64 (6) (2001) 4. doi:10.1103/PhysRevE.64.066604.

[10] B. van Tiggelen, L. Margerin, M. Campillo, Coherent backscattering of elastic waves: Specific role of source, polarization, and near field, J. Acoust. Soc. Am. 110 (3) (2001) 1291–1298. doi:10.1121/1.1388017.

[11] A. Tourin, A. Derode, P. Roux, B. A. van Tiggelen, M. Fink, Time-Dependent Coherent Backscattering of Acoustic Waves, Phys. Rev. Lett. 79 (19) (1997) 3637–3639. doi:10.1103/PhysRevLett.79.3637.

[12] Y. Zhang, O. Abraham, V. Tournat, A. Le Duff, B. Lascoup, A. Loukili, F. Grondin, O. Durand, Validation of a thermal bias control technique for coda wave interferometry (cwi), Ultrasonics 53 (3) (2013) 658–664. doi:https://doi.org/10.1016/j.ultras.2012.08.003.
URL https://www.sciencedirect.com/science/article/pii/S0041624X12001564

[13] F. Xie, E. Larose, L. Moreau, Y. Zhang, T. Planes, Characterizing extended changes in multiple scattering media using coda wave decorrelation: numerical simulations, Waves in Random and Complex Media 28 (1) (2018) 1–14. arXiv:https://doi.org/10.1080/17455030.2017.1308042, doi:10.1080/17455030.2017.1308042.
URL https://doi.org/10.1080/17455030.2017.1308042

[14] Y. Zhang, T. Planès, E. Larose, Obermann, Diffuse ultrasound monitoring of stress and damage development on a 15-ton concrete beam, J. Acoust. Soc. Am. 139 (4) (2016) 1691–1701. doi:10.1121/1.4945097.

[15] R. Zotz-Wilson, T. Boerrigter, A. Barnhoorn, Coda-wave monitoring of continuously evolving material properties and the precursory detection of yielding, J. Acoust. Soc. Am. 145 (2) (2019) 1060–1068. arXiv:1808.02732, doi:10.1121/1.5091012.

[16] R. Snieder, The theory of coda wave interferometry, Pure Appl. Geophys. 163 (2-3) (2006) 455–473. doi:10.1007/s00024-005-0026-6.

[17] P. Fröjd, P. Ulriksen, Frequency selection for coda wave interferometry in concrete structures, Ultrasonics 80 (2017) 1–8. doi:10.1016/j.ultras.2017.04.012.

[18] T. Planès, E. Larose, A review of ultrasonic Coda Wave Interferometry in concrete, Cem. Concr. Res. 53 (2013) 248–255. doi:10.1016/j.cemconres.2013.07.009.
URL http://dx.doi.org/10.1016/j.cemconres.2013.07.009

[19] G. Sang, S. Liu, D. Elsworth, Quantifying fatigue-damage and failure-precursors using ultrasonic coda wave interferometry, International Journal of Rock Mechanics and Mining Sciences 131 (January) (2020) 104366. doi:10.1016/j.ijrmms.2020.104366.
URL https://doi.org/10.1016/j.ijrmms.2020.104366

[20] B. Chen, M. Abdallah, P. Campistron, E. Moulin, D. Callens, S. O. Khelissa, P. Debreyne, N. E. Chihib, G. Delaplace, Detection of biofilm formation by ultrasonic Coda Wave Interferometry, Journal of Food Engineering 290 (May 2020) (2021) 110219. doi:10.1016/j.jfoodeng.2020.110219.
URL https://doi.org/10.1016/j.jfoodeng.2020.110219

[21] F. Xie, Y. Zhang, E. Larose, A. Duclos, S. Chen, X. Li, C. Fei, Characterizing mechanical change in metals using amplitude-modulated diffuse ultrasound, Structural Health Monitoring 19 (6) (2020) 1894–1904. doi:10.1177/1475921720905046.

[22] R. Snieder, A. Grêt, H. Douma, J. Scales, Coda wave interferometry for estimating nonlinear behavior in seismic velocity, Science (80-.). 295 (5563) (2002) 2253–2255. doi:10.1126/science.1070015.

[23] C. Payan, V. Garnier, J. Moysan, P. A. Johnson, Determination of third order elastic constants in a complex solid applying coda wave interferometry, Applied Physics Letters 94 (1). doi:10.1063/1.3064129.

[24] H. Hu, D. Li, L. Wang, R. Chen, X. Xu, An improved ultrasonic coda wave method for concrete behavior monitoring under various loading conditions, Ultrasonics 116 (April) (2021) 106498. doi:10.1016/j.ultras.2021.106498.
URL https://doi.org/10.1016/j.ultras.2021.106498

[25] B. Chen, D. Callens, P. Campistron, E. Moulin, P. Debreyne, G. Delaplace, Monitoring cleaning cycles of fouled ducts using ultrasonic coda wave interferometry (CWI), Ultrasonics 96 (October 2018) (2019) 253–260. doi:10.1016/j.ultras.2018.12.011.
URL https://doi.org/10.1016/j.ultras.2018.12.011

[26] O. I. Lobkis, R. L. Weaver, Coda-Wave Interferometry in Finite Solids: Recovery of P-to-S Conversion Rates in an Elastodynamic Billiard, Phys. Rev. Lett. 90 (25) (2003) 254302. doi:10.1103/PhysRevLett.90.254302.
URL https://link.aps.org/doi/10.1103/PhysRevLett.90.254302

[27] C. Sens-Schönfelder, U. Wegler, Passive image interferometry and seasonal variations of seismic velocities at merapi volcano, indonesia, Geophysical Research Letters 33 (21). arXiv:https://agupubs.onlinelibrary.wiley.com/doi/pdf/10.1029/2006GL027797, doi:https://doi.org/10.1029/2006GL027797.
URL https://agupubs.onlinelibrary.wiley.com/doi/abs/10.1029/2006GL027797

[28] L. Pahlavan, F. Zhang, G. Blacquière, Y. Yang, D. Hordijk, Interaction of ultrasonic waves with partially-closed cracks in concrete structures, Construction and Building Materials 167 (2018) 899–906. doi:https://doi.org/10.1016/j.conbuildmat.2018.02.098.
URL https://www.sciencedirect.com/science/article/pii/S0950061818303337

[29] B. Hilloulin, Y. Zhang, O. Abraham, A. Loukili, F. Grondin, O. Durand, V. Tournat, Small crack detection in cementitious materials using nonlinear coda wave modulation, NDT E Int. 68 (2014) 98–104. doi:10.1016/j.ndteint.2014.08.010.
URL http://dx.doi.org/10.1016/j.ndteint.2014.08.010

[30] J.-B. Legland, Y. Zhang, O. Abraham, O. Durand, V. Tournat, Evaluation of crack status in a meter-size concrete structure using the ultrasonic nonlinear coda wave interferometry, J. Acoust. Soc. Am. 142 (4) (2017) 2233–2241. doi:10.1121/1.5007832.

[31] G. Chen, Y. Zhang, O. Abraham, D. Pageot, M. Chekroun, V. Tournat, Numerical parametric study of nonlinear coda wave interferometry sensitivity to microcrack size in a multiple scattering medium, Ultrasonics 116 (2021) 106483. doi:https://doi.org/

10.1016/j.ultras.2021.106483.
URL https://www.sciencedirect.com/science/article/pii/S0041624X2100113X

[32] G. Chen, D. Pageot, J.-B. Legland, O. Abraham, M. Chekroun, V. Tournat, Numerical modeling of ultrasonic coda wave interferometry in a multiple scattering medium with a localized nonlinear defect, Wave Motion 72 (2017) 228–243. doi:https://doi.org/10.1016/j.wavemoti.2017.03.004.
URL https://www.sciencedirect.com/science/article/pii/S016521251730032X

[33] G. Chen, D. Pageot, O. Abraham, Y. Zhang, M. Chekroun, V. Tournat, Nonlinear coda wave interferometry: Sensitivity to wave-induced material property changes analyzed via numerical simulations in 2d, Ultrasonics 99 (2019) 105968. doi:10.1016/j.ultras.2019.105968.

[34] J.-B. Legland, O. Abraham, O. Durand, J. M. Henault, Monitoring localized cracks on under pressure concrete nuclear containment wall using linear and nonlinear ultrasonic coda wave interferometry, AIP Conf. Proc. 1949. doi:10.1063/1.5031646.

[35] Y. Zhang, E. Larose, L. Moreau, G. D'Ozouville, Three-dimensional in-situ imaging of cracks in concrete using diffuse ultrasound, Struct. Heal. Monit. 17 (2) (2018) 279–284. doi:10.1177/1475921717690938.

[36] Y. Zhang, T. Planès, E. Larose, A. Obermann, C. Rospars, G. Moreau, Diffuse ultrasound monitoring of stress and damage development on a 15-ton concrete beam, The Journal of the Acoustical Society of America 139 (4) (2016) 1691–1701. arXiv:https://doi.org/10.1121/1.4945097, doi:10.1121/1.4945097.
URL https://doi.org/10.1121/1.4945097

[37] Y. Zhang, V. Tournat, O. Abraham, O. Durand, S. Letourneur, A. Le Duff, B. Lascoup, Nonlinear coda wave interferometry for the global evaluation of damage levels in complex solids, Ultrasonics 73 (2017) 245–252. doi:https://doi.org/10.1016/j.ultras.2016.09.015.
URL https://www.sciencedirect.com/science/article/pii/S0041624X16301950

[38] A. Obermann, T. Planes, E. Larose, M. Campillo, 4-d imaging of subsurface changes with coda waves: Numerical studies of 3-d combined sensitivity kernels and applications to the mw 7.9, 2008 wenchuan earthquake, Pure and Applied Geophysicsdoi:10.1007/s00024-018-2014-7.

[39] F. Xie, L. Moreau, Y. Zhang, E. Larose, A bayesian approach for high resolution imaging of small changes in multiple scattering media, Ultrasonics 64 (2016) 106–114. doi:https://doi.org/10.1016/j.ultras.2015.08.005.
URL https://www.sciencedirect.com/science/article/pii/S0041624X15002152

[40] T. Planès, E. Larose, V. Rossetto, L. Margerin, Imaging multiple local changes in heterogeneous media with diffuse waves, The Journal of the Acoustical Society of America 137 (2) (2015) 660–667. arXiv:https://doi.org/10.1121/1.4906824,

doi:10.1121/1.4906824.
URL https://doi.org/10.1121/1.4906824

[41] B. Van Belleghem, K. Van Tittelboom, N. De Belie, Efficiency of self-healing cementitious materials with encapsulated polyurethane to reduce water ingress through cracks, Mater. Constr. 68 (330). doi:10.3989/mc.2018.05917.

[42] B. Lubelli, T. G. Nijland, R. P. Van Hees, Self-healing of lime based mortars: Microscopy observations on case studies, Heron 56 (1-2) (2011) 81–97.

[43] P. Y. Le Bas, M. C. Remillieux, L. Pieczonka, J. A. Ten Cate, B. E. Anderson, T. J. Ulrich, Damage imaging in a laminated composite plate using an air-coupled time reversal mirror, Appl. Phys. Lett. 107 (18). doi:10.1063/1.4935210.
URL http://dx.doi.org/10.1063/1.4935210

[44] T. Planès, E. Larose, V. Rossetto, L. Margerin, Imaging multiple local changes in heterogeneous media with diffuse waves, J. Acoust. Soc. Am. 137 (2) (2015) 660–667. doi:10.1121/1.4906824.

[45] V. Rossetto, L. Margerin, T. Planès, É. Larose, Locating a weak change using diffuse waves: Theoretical approach and inversion procedure, J. Appl. Phys. 109 (3). arXiv:1007.3103, doi:10.1063/1.3544503.

[46] Q. Xue, E. Larose, L. Moreau, Locating structural changes in a multiple scattering domain with an irregular shape, J. Acoust. Soc. Am. 146 (1) (2019) 595–602. doi:10.1121/1.5118246.

[47] L. Margerin, T. Planes, J. Mayor, M. Calvet, Sensitivity kernels for coda-wave interferometry and scattering tomography: Theory and numerical evaluation in two-dimensional anisotropically scattering media, Geophysical Journal International 204 (2016) 650–666. doi:10.1093/gji/ggv470.

[48] N. Smagin, A. Trifonov, O. Bou Matar, V. Aleshin, Local damage detection by nonlinear coda wave interferometry combined with time reversal, Ultrasonics 108 (2020) 106226. doi:https://doi.org/10.1016/j.ultras.2020.106226.
URL https://www.sciencedirect.com/science/article/pii/S0041624X20301657

[49] D. Brill, G. Gaunaurd, Resonance theory of elastic waves ultrasonically scattered from an elastic sphere, The Journal of the Acoustical Society of America 81 (1) (1987) 1–21. arXiv:https://doi.org/10.1121/1.394983, doi:10.1121/1.394983.
URL https://doi.org/10.1121/1.394983

[50] G. Johnson, R. Truell, Numerical computations of elastic scattering cross sections, Journal of Applied Physics 36 (11) (1965) 3466–3475. arXiv:https://doi.org/10.1063/1.1703020, doi:10.1063/1.1703020.
URL https://doi.org/10.1063/1.1703020

[51] V. A. Korneev, L. R. Johnson, Scattering of elastic waves by a spherical inclusion—I. Theory and numerical results, Geophysical Journal International 115 (1) (1993) 230–250. arXiv:https://academic.oup.com/gji/article-pdf/115/1/230/1654670/115-1-230.pdf, doi:10.1111/j.1365-246X.1993.tb05601.x.
URL https://doi.org/10.1111/j.1365-246X.1993.tb05601.x

[52] C. C. Mow, Y. H. Pao, The Diffraction of Elastic Waves and Dynamic Stress Concentrations, RAND Corporation, Santa Monica, CA, 1971.

[53] A. Quiviger, A. Girard, C. Payan, J. F. Chaix, V. Garnier, J. Salin, Influence of the depth and morphology of real cracks on diffuse ultrasound in concrete: A simulation study, NDT E Int. 60 (2013) 11–16. doi:10.1016/j.ndteint.2013.07.003.

[54] C. Sens-Schönfelder, R. Snieder, X. Li, A model for nonlinear elasticity in rocks based on friction of internal interfaces and contact aging, Geophys. J. Int. 216 (1) (2019) 319–331. doi:10.1093/gji/ggy414.

[55] R. Snieder, C. Sens-Schönfelder, R. Wu, The time dependence of rock healing as a universal relaxation process, a tutorial, Geophys. J. Int. 208 (1) (2017) 1–9. doi:10.1093/gji/ggw377.

[56] D. Komatitsch, J. P. Vilotte, The spectral-element method: an efficient tool to simulate the seismic response of 2D and 3D geological structures, Bulletin of the Seismological Society of America 88 (2) (1998) 368–392.
URL https://hal.inria.fr/hal-00669068

[57] D. Komatitsch, J.-P. Vilotte, R. Vai, J. M. Castillo-Covarrubias, F. J. Sánchez-Sesma, The spectral element method for elastic wave equations—application to 2-d and 3-d seismic problems, International Journal for Numerical Methods in Engineering 45 (9) (1999) 1139–1164.

[58] F. Hecht, New development in freefem++, Journal of Numerical Mathematics 20 (3-4) (2012) 251–266. doi:doi:10.1515/jnum-2012-0013.
URL https://doi.org/10.1515/jnum-2012-0013

[59] Y. Zhang, V. Tournat, O. Abraham, O. Durand, S. Letourneur, A. Le Duff, B. Lascoup, Nonlinear mixing of ultrasonic coda waves with lower frequency swept pump waves for global detection of defects in multiple scattering media, Journal of Applied Physics 113 (2013) 064905. doi:10.1063/1.4791585.

[60] D. Komatitsch, J.-P. Vilotte, The spectral element method: An efficient tool to simulate the seismic response of 2D and 3D geological structures, Bulletin of the Seismological Society of America 88 (2) (1998) 368–392. arXiv:https://pubs.geoscienceworld.org/ssa/bssa/article-pdf/88/2/368/5344788/bssa0880020368.pdf, doi:10.1785/BSSA0880020368.
URL https://doi.org/10.1785/BSSA0880020368

[61] E. Chaljub, D. Komatitsch, J.-P. Vilotte, The spectral element method: An efficient tool to simulate the seismic response of 2-d and 3-d geological structures, Bulletin of the Seismological Society of America 88.

[62] E. Chaljub, D. Komatitsch, J.-P. Vilotte, Y. Capdeville, B. Valette, G. Festa, Spectral-element analysis in seismology, in: R.-S. Wu, V. Maupin, R. Dmowska (Eds.), Advances in Wave Propagation in Heterogenous Earth, Vol. 48 of Advances in Geophysics, Elsevier, 2007, pp. 365–419. doi:https://doi.org/10.1016/S0065-2687(06)48007-9.
URL https://www.sciencedirect.com/science/article/pii/S0065268706480079

[63] F. van de Vosse, P. Minev, Spectral Element Methods: Theory and Applications, EUT report, Eindhoven University of Technology, Faculty of Mechanical Engineering, 1996.
URL https://books.google.fr/books?id=9ZZKtwAACAAJ

[64] M. Azaiez, M. Dauge, Y. Maday, Méthodes spectrales et des eléments spectraux, Technical Report 17, Institut de Recherche mathématique de Rennes, Université de Rennes I.
URL https://www.researchgate.net/publication/264843516_Methodes_Spectrales_et_des_Elements_Spectraux

[65] P. Blanloeuil, A. Meziane, C. Bacon, Numerical study of nonlinear interaction between a crack and elastic waves under an oblique incidence, Wave Motion 51 (3) (2014) 425–437. doi:https://doi.org/10.1016/j.wavemoti.2013.10.002.
URL https://www.sciencedirect.com/science/article/pii/S0165212513001613

[66] P. Blanloeuil, A. J. Croxford, A. Meziane, Numerical and experimental study of the nonlinear interaction between a shear wave and a frictional interface, The Journal of the Acoustical Society of America 135 (4) (2014) 1709–1716. doi:10.1121/1.4868402.
URL https://doi.org/10.1121/1.4868402

[67] W. Curtis, J. Logan, W. Parker, Dimensional analysis and the pi theorem, Linear Algebra and its Applications 47 (1982) 117–126. doi:https://doi.org/10.1016/0024-3795(82)90229-4.
URL https://www.sciencedirect.com/science/article/pii/0024379582902294

Appendices

A. Nomenclature

	Variable	Description
Acoustical parameters	$u_i(t)$	reference coda signal
	$u_p(t)$	perturbed coda signal
	$CC(\theta)$	correlation coefficient between $u_i(t)$ and $u_p(t)$ for a given θ
	θ	relative velocity change of the elastic medium
	K_d	decorrelation coefficient between reference and perturbed coda signals
	α_θ	coefficient of linear term of θ vs. pump wave stress amplitude
	α_{K_d}	coefficient of quadratic term of K_d vs. pump wave stress amplitude
	σ_D	scattering cross section of the crack
	$\sigma_{dyn}(t)$	time signal of the dynamic pump waves
	σ_{dyn}^{max}	maximum dynamic pump stress wave amplitude of $\sigma_{dyn}(t)$
	V_p	velocity of pressure waves
	V_s	velocity of shear waves
Material parameters	E	Young's modulus
	ν	Poisson's ratio
	ρ	density
Static model parameters	L_{medium}	length of the rectangular medium
	D	height of the rectangular medium
	L	length of the crack
	h	aperture at the crack center
	y_{geo}	function of the crack surface geometry
	u_x	horizontal displacement of the crack surface
	u_y	vertical displacement of the crack surface
	dL	algebraic length variation of the open part of the crack
	dL^{pre}	pre-close crack segment
	$dL^{\pm}$	length variation of the open part of the crack (dL^+: opening, dL^-: closure)
	$[dL/L]_{dyn}(t)$	dynamic time variation of dL/L to $\sigma_{dyn}(t)$
	$\widetilde{dL/L}$	average of $[dL/L]_{dyn}(t)$ over time
	ω	limit aperture above which the crack is considered as open
	dx	distance between node O and node S of the crack
	Ω	2D elastic isotropic rectangular medium
	$\widetilde{\Omega}$	Upper right quarter of the medium
	Γ_L	embedded horizontal crack
	$\Gamma_{(L-dL)/2}$	open part of Γ_L
	$\Gamma_{dL/2}$	close part of Γ_L
	$\wp$	total problem of the FE crack model
	$\wp_1$	problem 1 of the FE crack model
	$\wp_2$	problem 2 of the FE crack model
	σ_0	far field stress applied on the crack in $\wp$
	γ	target value of σ_0
	$\boldsymbol{\sigma^{ff}}$	tensor of far field stress
	$\boldsymbol{T}$	traction vector

B. Detailed description of the pump / crack interaction (static model)

B.1. Relative crack length variation under far field stress loading in 2D plane strain

This part examines the equivalent effect of the dynamic pump wave over a crack during NCWI assuming static regime. As illustrated in Fig.B.1 (a), due to symmetries, a quarter of the elastic isotropic 2D domain Ω of dimension $L_{medium} \times D$ with an embedded horizontal crack Γ_L of length L is considered. The design of the crack geometry is illustrated in Fig.B.1 (b) and consists in two parts: an open segment AV and a pre-close segment VV'. this partially closed crack is used to model both crack closure and opening. The geometry of the crack surface along the open part is given by $y = \pm y_{geo(x)} = \pm\frac{h}{4}(1+\cos(\pi\frac{2x}{L}))$ with $0 \leq x \leq L/2$, $0 \leq y_{geo} \ll D$ and $y_{geo}(-x) = y_{geo}(x)$. The half length of the pre-close part is $dL^{pre}/2$. Domain Ω is subjected to a far field stress state on its outer boundary $\partial\Omega/\Gamma_L$ resulting in the traction vector $\boldsymbol{T}$:

$$\boldsymbol{T} = \boldsymbol{\sigma^{ff}} \cdot \boldsymbol{n}, \quad with \quad \boldsymbol{\sigma^{ff}} = \begin{bmatrix} \sigma_{xx}^{ff} & \sigma_{xy}^{ff} \\ \sigma_{yx}^{ff} & \sigma_{yy}^{ff} \end{bmatrix}, \tag{B.1}$$

The configuration in Fig.B.1 can treat both compressive and tensile stress. This stress at the domain boundaries, especially the σ_{yy}^{ff} component if non zero, is likely to induce a crack length variation of $dL^{\pm}/2$ due to compression or tension from each of its tips. The purpose of this section is to compute $dL^{\pm}/2$ as a function of $\boldsymbol{\sigma^{ff}}$, under the assumption of plane strain. $\Gamma_{(L-dL)/2}$ and $\Gamma_{dL/2}$ are denoted as the open and closed parts of the crack respectively.

First, it can be noticed that σ_{xx}^{ff} and σ_{xy}^{ff} do not or only barely affect the relative crack length variation. Indeed, assuming that σ_{xy} is zero on the whole crack length even on $\Gamma_{dL/2}$ (i.e. case of negligible contact friction conditions between the two crack surfaces), the change in the vertical displacement induced by can be calculated incrementally within the framework of linear elasticity. Therefore, owing to problem symmetry, the vertical displacement δu_y due to σ_{xx}^{ff} is zero on the x-axis, thus σ_{xx}^{ff} does not affect the crack closure. Also, due to symmetry, σ_{xy}^{ff} leads to similar vertical displacements on both crack surfaces, consequently not changing the existing aperture between the two surfaces.

Hence, only the effect of the component σ_{yy}^{ff} will be considered in the following discussion. In addition, we assume in the following that the closing length $dL/2$ is given, while the corresponding value of σ_{yy}^{ff} denoted $\sigma_{yy}^{ff}(dL/2)$ is considered as the unknown variable to be determined.

B.2. Adimensional analysis

The adimensional analysis aims to reduce the number of variables in order to simplify the parametric study in the following. In our problem, the relative crack length variation $\widetilde{dL/L}$ depends on several variables: E (Young's modulus), σ_{yy}^{ff}, L, dL^{pre}, h, ν (Poisson's ratio), which can be written as :

$$\begin{aligned} dL^{-} &= f(E, \sigma_{yy}^{ff}, L, h, \nu), \\ dL^{+} &= g(E, \sigma_{yy}^{ff}, L, dL^{pre}, h, \omega, \nu). \end{aligned} \tag{B.2}$$

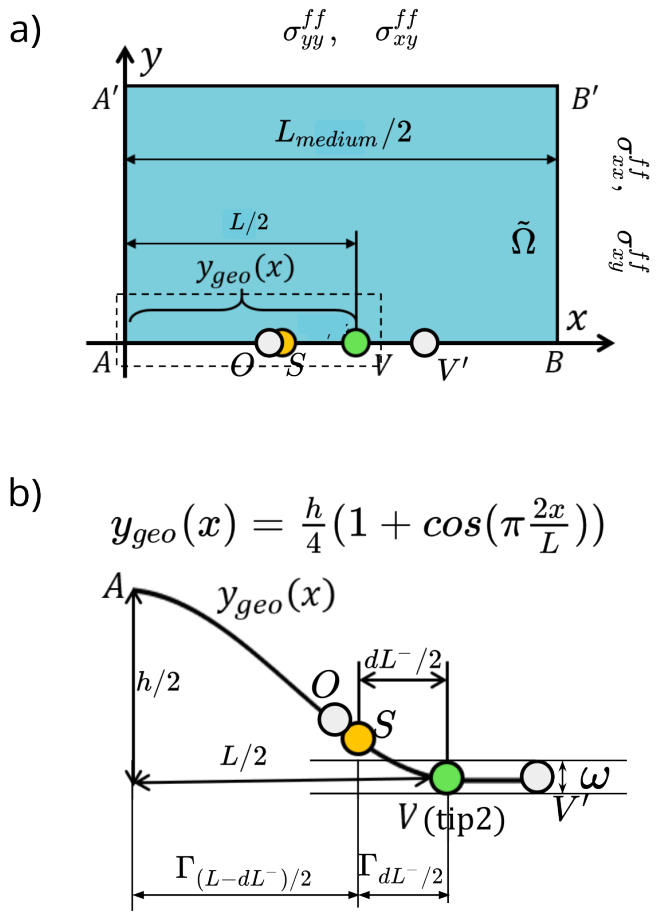

Figure B.1: Schematic representations of the static model :a) Upper right quarter the finite 2D rectangular domain Γ of dimension $L_{medium} \times D$ with a partially closed crack Γ_L centered at the center point A, the 2D domain is subjected to a far field stress $\boldsymbol{\sigma^{ff}}$ on the boundaries, the segment VA represents a half of total crack length, S is the anticipated new crack tip after the closure of $dL^-/2$, $V'V$ of length dL^{pre} represents the extension of AV whose initial aperture is 0, dL^- represents the crack closure length. b) Zoom over the crack segment $V'A$, the geometry of the half crack VA is described by $y_{geo}(x)$. O is an additional node placed at a small distance dx at left side of S. This node is used as a "testing node" in the FEM computation to help approximate the double contact condition to be checked in S, that is geometrical closure of the crack and zero normal stress.

According to Buckingham π theorem [67], Eq.B.2 can be reduced to an adimensional form :

$$\begin{aligned} \frac{dL^-}{L} &= F(\frac{\sigma^{ff}_{yy}}{E}, \frac{h}{L}, \nu), \\ \frac{dL^+}{L} &= G(\frac{\sigma^{ff}_{yy}}{E}, \frac{dL^{pre}}{L}, \frac{h}{L}, \frac{\omega}{h}, \nu). \end{aligned} \tag{B.3}$$

Supposing that ν is fixed, this static model can then be analysed by the 5 adimensional parameters: $\widetilde{dL/L}$, dL^{pre}/L, σ^{ff}_{yy}/E, h/L and ω/h. The dynamic pump wave has both positive and negative amplitudes, these correspond to compression and tension respectively. Hence, two cases are considered in the static model: crack closure and crack opening. The first case is solved by using a sub-problem decomposition method.

The second one is solved by applying an external tensile load on the boundaries with the application of crack opening criteria ω.

C. Crack closure and crack opening modeling

C.1. Crack closure: sub-problem decomposition

The process of sub-problem decomposition is presented in Fig.C.1. The total problem $\wp$ (Fig.C.1(a)) describes the crack surface deformation under arbitrary far field tensile stress σ_{yy}^{ff} (or σ_0), which can be solved numerically using the standard Finite Element method. In the sub-problem decomposition, the total problem $\wp$ is decomposed into two sub-problems $\wp_1$ and $\wp_2$. The first sub-problem $\wp_1$ describes the crack surface deformation under a reference far field tensile stress σ_{yy1}^{ff}. The second sub-problem $\wp_2$ describes the crack surface deformation due to the application of a normal displacement $u_y(x)$ opposite to $y_{geo}(x)$ which makes it possible to close the crack along SV. Since the crack aperture h is negligible in front of the size of the medium Ω, hence in the FE modeling, the crack segment AV is geometrically represented by a straight line confounded with the x axis. $\tilde{\Omega}$ is the upper right part of the structure $0 \leq x \leq L_{medium}/2, 0 \leq y \leq D/2$, O the point with coordinates $(x = (L - dL^-)/2 - dx, y = 0^+)$, S the point with coordinates $(x = (L - dL^-)/2, y = 0^+)$, where dx has the size of one or several mesh elements in this area. S and O as nodes are included in mesh nodes. As mentioned in Fig.B.1 that O is a "testing node" to approximate the double contact condition, the nodal point S is actually the real left ending point of the crack closure segment. Since only one of the double contact condition (e.g. zero aperture and zero normal stress) can be applied on a nodal point, it can happen, due to numerical error, that the eventual aperture on the chosen nodal point is zero while the normal stress is non zero, or the normal stress is zero but the aperture is non zero. Therefore, The application of the contact condition (zero aperture in our case) on point O, which is at the left side of S by a very small distance dx, is to test if both double contact condition are satisfied. If so, then the point S can be taken as the left ending point of the crack closure segment. $\tilde{\Gamma}_{dL^-/2}$ is the set of the nodes located on the right half part of $\Gamma_{dL^-/2}$ except point O $(x < (L - dL^-)/2, y = 0^+)$. All boundary conditions are presented in Table.C.1. For both problems $\wp_1$ and $\wp_2$, the nodal vertical displacement at point O ($u_{y1}(O)$ and $u_{y2}(O)$) is considered as free, while the corresponding nodal vertical force is set equal to 0. For $\wp_2$ the nodal vertical displacements of $\tilde{\Gamma}_{dL^-/2}$ are taken as equal to the nodal values of $-y_{geo}$, while these are set to zero for $\wp_1$. On the upper limit Γ_{sup} of $\tilde{\Omega}$, the stress component σ_{yy}^{ff} is set at 1 MPa for $\wp_1$, denoted as σ_{yy1}^{ff} and equal to 0 for $\wp_2$, denoted as σ_{yy2}^{ff}. All other boundary conditions of $\wp_1$, $\wp_2$ (zero displacement or stress components) are the same for both problems and assumed to be identical to those of $\wp$. At the output, $\wp_1$ and $\wp_2$ give the nodal vertical displacements at point O $u_{y1}(O)$ and $u_{y2}(O)$ respectively.

It then becomes straightforward to verify, from the boundary conditions of $\wp$, that the problem can be obtained as the following superposition:

$$\wp = \gamma\wp_1 + \wp_2, \tag{C.1}$$

Table C.1: Boundary conditions applied on all segments in problem 1 and 2.

Segment	Problem 1	Problem 2
AA'	$u_x = 0$, $\sigma_{xy} = 0$	$u_x = 0$, $\sigma_{xy} = 0$
A'B'	$\sigma_{yy} = 1$MPa (along $-\boldsymbol{y}$), $\sigma_{xy} = 0$	$\sigma_{yy} = 0$, $\sigma_{xy} = 0$
B'B	$\sigma_{xx} = 1$MPa (along $-\boldsymbol{x}$), $\sigma_{xy} = 0$	$\sigma_{xx} = 0$, $\sigma_{xy} = 0$
VB	$u_y = 0$, $\sigma_{xy} = 0$	$u_y = 0$, $\sigma_{xy} = 0$
SV	$u_y = 0$, $\sigma_{xy} = 0$	$u_y = -y_{geo}(x)$, $\sigma_{xy} = 0$
AO&OS	$\sigma_{yy} = 0$, $\sigma_{xy} = 0$	$\sigma_{yy} = 0$, $\sigma_{xy} = 0$

where γ represents the target value of the far field stress σ_0 (in MPa) needed for a crack closure of dL^-. Provided that the total vertical displacement u_y of point O equals zero, and the crack segment AV a straight line. The boundary conditions in $\wp_1$ and $\wp_2$ also lead automatically to zero normal stress at O. Therefore, u_y at point O of $\wp$ should equal to $-y_{geo}(O)$. This set-up leads to the target value γ, namely:

$$\begin{aligned} -y_{geo}(O) &= \gamma u_{y1}(O) + u_{y2}(O), \\ \gamma &= -[u_{y2}(O) + y_{geo}(O)]/u_{y1}(O), \end{aligned} \tag{C.2}$$

where $u_{y1}(O)$, $u_{y2}(O)$ are the vertical displacements of point O computed for $\wp_1$ and $\wp_2$ using the Finite Element method.

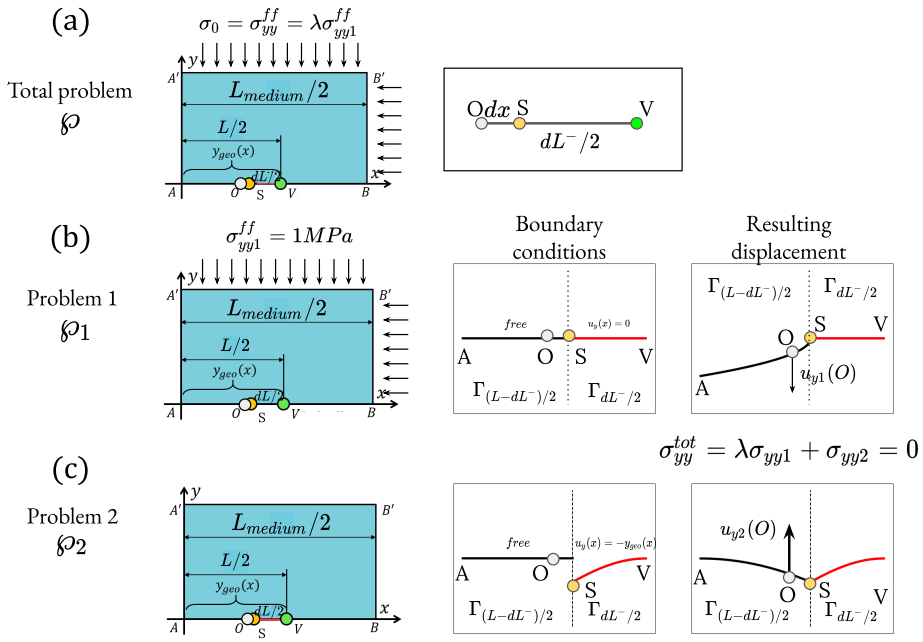

Figure C.1: Schematics of total problem $\wp$, problem 1 $\wp_1$ and problem 2 $\wp_2$ of the crack closure process. The initial half crack is represented by VA and the anticipated half crack closure length $dL^-/2$ is represented by VS. (a). Total problem: glass plate under biaxial static stress load σ_{dyn}^{max} which allows a zero normal stress and crack aperture at point O ($x = (L - dL^-)/2 - dx$). (b). Problem 1: the plate is under biaxial static stress load σ_{yy1}^{ff}=1MPa, the normal displacement u_y along SV is restricted to be zero. (c). Problem 2: the plate is free from external load, the normal displacement u_y along SV is imposed to be the opposite of the initial crack geometry, thus $-y_{geo}(x)$.

C.2. Crack opening

As illustrated in Fig.3, since $V'V$ is defined as a pre-close segment without prestress (self-stress state), $V'V$ will be completely open as soon as a tensile stress is applied. However the crack length grows gradually with the increase of the tensile load in the real crack opening. Therefore, a limit aperture ω is introduced, only the crack surface whose aperture above ω is considered as open. Denoting the normal displacement along the crack segment AV' due to the external far field tensile stress load σ_{yy}^{ff} as $u_y(x)$, dL^+/L is determined by satisfying the following condition (abscissa for which the crack displacement is equal to ω):

$$u_y(x = (L + dL^+)/2) = \omega. \tag{C.3}$$

The normal crack surface displacement $u_y(x)$ caused by a far field normal tensile stress σ_{yy}^{ff} can be obtained by 2 steps. First, applying a reference far field tensile stress which gives a reference normal crack surface displacement $u_y^{ref}(x)$. Then, since the elastic medium is considered as linear, for any σ_{yy}^{ff}, there is:

$$u_y(x) = \sigma_{yy}^{ff} u_y^{ref}(x). \tag{C.4}$$

Combining Eq.C.3 and Eq.C.4 gives:

$$\sigma_{yy}^{ff} = \omega / u_y^{ref}(x = (L + dL^+)/2). \tag{C.5}$$

Since $u_y^{ref}(x)$ is obtained in advance from numerical modeling, dL^+ can then be determined implicitly for given values of σ_{yy}^{ff} and ω.